Revista Univap
CIÊNCIA • TECNOLOGIA • HUMANISMO
Uma publicação da Universidade do Vale do Paraíba | Desde 1993 • Publicação contínua

EVALUATION OF COATED TI-6AL-4V ALLOY WITH WC-CO-CR BY CO2 LASER POWDER BED FUSION (L-PBF)

AVALIAÇÃO DA LIGA TI-6AL-4V REVESTIDA COM WC-CO-CR POR FUSÃO EM LEITO DE PÓ A LASER DE CO2 (L-FLP)

EVALUACIÓN DE LA ALEACIÓN TI-6AL-4V RECUBIERTA CON WC-CO-CR MEDIANTE FUSIÓN DE LECHO DE POLVO CON LÁSER CO2 (L-FLP)

Silvelene Alessandra Silva[1]
Vitor Ribeiro Jardim[2]
Paulo Paiva Oliveira Leite Dyer[3]
Renê Martins Volú[4]
Ana Cláudia Costa de Oliveira[5]
Getulio de Vasconcelos[6]

Abstract: The Ti-6Al-4V alloy with tungsten carbide as a coating combines the unique properties of these two materials to create a surface of high strength and durability. In this paper, the deposition of cobalt-bonded tungsten carbide composite (WC-Co-Cr) was sprayed through the pneumatic gun on a titanium-based alloy (Ti-6Al-4V) substrate, and after irradiation by CO_2 laser, by the laser powder bed fusion (L-PBF) method. To evaluate the operating parameters and coating mechanical and elemental properties. To this end, a 70 W CO_2 laser was used to irradiate the pre-deposited WC-Co-Cr powder with an energy density of 7×10^4 W/cm². Considering laser parameters, the best results were obtained for a beam scanning velocity of about 30 mm/s. It was observed that the metallurgical bond between coating and substrate promotes a strong adhesion between them. In addition, regions with a fully dense deposited layer thickness of 20 μm were observed. However, the presence of pores due to trapped WC decarburization gases was verified. Despite this issue and others, such as cracks, the coating showed a substantial increase in surface hardness, a significant decrease in the friction coefficient, and a significant reduction in wear rate.
Key words: CO_2 L-PBF; WC-Co-Cr; Aeronautical titanium alloy; Ti-alloy wear resistance increasing.

Resumo: A liga Ti-6Al-4V com carboneto de tungsténio como revestimento combina as propriedades únicas desses dois materiais para criar uma superfície de alta resistência e durabilidade. Neste artigo, a deposição do composto de carboneto de tungsténio ligado a cobalto (WC-Co-Cr) foi pulverizada através da pistola pneumática sobre um substrato de liga à base de titânio (Ti-6Al-4V) e, após irradiação por laser de CO_2, pelo método de fusão a laser em leito de pó (L-FLP).

[1] **Instituto de Estudos Avançados - INPE. E-mail: lenisoni@uol.com.br**
[2] **Instituto de Estudos Avançados - INPE. E-mail: vitorribeiroj@gmail.com**
[3] **Instituto de Estudos Avançados - INPE. E-mail: paulo_dyer@yahoo.com**
[4] **Instituto de Estudos Avançados - INPE. E-mail: rmvolu@gmail.com**
[5] **Universidade Federal de Lavras. E-mail: aclaudiacosta21@gmail.com**
[6] **Instituto de Estudos Avançados - INPE. E-mail: getuliovas@gmail.com**

Para avaliar os parâmetros operacionais e as propriedades mecânicas e elementares do revestimento. Para tal, foi utilizado um laser de CO_2 de 70 W para irradiar o pó WC-Co-Cr pré-depositado com uma densidade de energia de 7×10^4 W/cm². Considerando os parâmetros do laser, os melhores resultados foram obtidos para uma velocidade de varredura do feixe de cerca de 30 mm/s. Observou-se que a ligação metalúrgica entre o revestimento e o substrato promove uma forte adesão entre eles. Além disso, foram observadas regiões com uma espessura de camada depositada totalmente densa de 20 µm. No entanto, foi verificada a presença de poros devido a gases de descarbonização WC aprisionados. Apesar deste problema e de outros, tais como fissuras, o revestimento apresentou um aumento substancial na dureza da superfície, uma diminuição significativa no coeficiente de atrito e uma redução significativa na taxa de desgaste
Palavras-chave: L-FLP laser de CO_2; WC-Co-Cr; Liga de titânio aeronáutica; Liga de titânio com aumento da resistência ao desgaste.

Resumen: La aleación Ti-6Al-4V con carburo de tungsteno como recubrimiento combina las propiedades únicas de estos dos materiales para crear una superficie de alta resistencia y durabilidad. En este trabajo, la deposición del compuesto de carburo de tungsteno ligado con cobalto (WC-Co-Cr) se pulverizó a través de la pistola neumática sobre un sustrato de aleación con base de titanio (Ti-6Al-4V), y después de la irradiación por láser de CO_2, por el método de fusión de lecho de polvo láser (L-PBF). Evaluar los parámetros de funcionamiento y las propiedades mecánicas y elementales del recubrimiento. Para ello, se utilizó un láser de CO_2 de 70 W para irradiar el polvo de WC-Co-Cr pre-depositado con una densidad de energía de 7×10^4 W/cm². Teniendo en cuenta los parámetros del láser, los mejores resultados se obtuvieron para una velocidad de barrido del haz de unos 30 mm/s. Se observó que la unión metalúrgica entre el revestimiento y el sustrato favorece una fuerte adhesión entre ambos. Además, se observaron regiones con un espesor de capa depositada totalmente densa de 20 µm. Sin embargo, se verificó la presencia de poros debidos a gases de descarburación del WC atrapados. A pesar de este problema y de otros, como grietas, el recubrimiento mostró un aumento sustancial de la dureza superficial, una disminución significativa del coeficiente de fricción y una reducción significativa de la tasa de desgaste
Palabras clave: L-FLP con láser CO_2; WC-Co-Cr; Aleación de titanio para aeronáutica; Aleación de titanio con mayor resistencia al desgaste.

1 INTRODUCTION

Titanium and its alloys are extensively used in the aeronautical, engineering, and biomedical sectors due to their high strength-to-weight ratio, excellent corrosion resistance, and thermal conductivity. In contrast, a low wear resistance. In this context, a coating process applied to these alloys is welcomed to improve this aspect (Makurat-Kasprolewicz & Ossowska, 2023; Rominiyi & Mashinini, 2024).

According to El-Hamid et al. (2024), the coating material properties, such as a ceramic with high wear resistance on the interest substrate, could transfer its properties to the formed composite (coated substrate). Although poor adherence compromises this set, it generates surface defects and residual stress. In this way, Yetim et al. (2010) explain this difficulty. However, this issue can be overcome by metallic matrix ceramics deposited by high-energy methods, such as laser powder bed fusion (L-PBF). The laser beam assures a well-anchorage between the ceramic's metal matrix and substrate, incorporating the ceramic into a formed composite.

The wear improvement can expand the applications of titanium alloys. The aerospace sector stands out, considering the number of sensitive parts with high levels of safety assurance, as turbine vanes, landing gear, and aircraft structural components (Lisiecki & Klimpel, 2008; Zhao et al., 2023). According to Moskalewicz et al. (2010), these parts are constantly subjected to high levels of stress and thermal variation, and must fulfill the EN 9100 (European Committee for Standardization [CEN], 2018). Besides its mechanical properties, this use brings economic benefits to airline companies; due to its 60% lower specific mass compared to steel alloys (Makurat-Kasprolewicz & Ossowska, 2023). Kaufmann et al. (2008) emphasize a saving of about $3,000 for each kilogram reduction. With this, the strength/weight ratio of Ti-6Al-4V contributes both to part reliability and its benefit-cost (Zwerdeling, 2013).

Pawlowski (2008), Obadele et al. (2015), and Kummel et al. (2020) point out that the use of metal-ceramic as a coating (coating powder mixture) is widely applied to improve. Highlighting the cemented carbides by metallic matrix (Co or Ni) with ceramic particles, such as tungsten carbides (WC), hard and withstanding high temperatures, due to refractory phases (Callister Jr. & Rethwisch, 2014). With this, the metallic matrix acts as a ‘binder’ (incorporating the ceramic), allowing the metallurgical bonding with the substrate. With this, these coating powders are indicated for titanium alloys.

Notwithstanding, there remains a great difficulty in anchoring these coating powders by flame-spray (FSD), plasma spray (PS-PVD), high velocity oxy-fuel flame (HVOF), and other aspersion methods and techniques; due to high materials fusion temperatures (Rominiyi & Mashinini, 2024). In this way, Obadele et al. (2015), Steen and Mazumder (2010) highlight the success of the L-PBF method to assure the metallurgical bonding between the ceramic's binder and substrate. In other words, explain Figueira et al. (2022), the laser beam provides a high volumetric-energy-density or ‘*VED*’ (over 91.4 J/mm³) capable of simultaneously melting coat-powder and substrate. This allows diffusion between the two materials, with solidification of the formed alloy, thus characterized as a metallurgical bonding. To this end, states Li et al. (2020), the experiment parameters must be adjusted to obtain the desired result, such as: beam diameter; or spot; ‘b_d’ (in mm), laser power ‘*P*’ (in W), velocity of scanning ‘v_s’ (in mm/s) of laser beam displacement and thickness of the pre-deposited powder bed 'T_k' (or pre-deposited powder, or cold spray deposited film). Thus, each experiment has specific laser irradiation parameters for L-PBF,

depending on coating and substrate properties (Dutta Majumdar & Manna, 2011). In this way, literature shows possible parameters' horizon, considering L-PBF equipment specifications and metallic substrates. Nevertheless, some research opportunities in the ambit of v_s, P, T_k, and generated thermally affected zone 'HAZ' (which refers to the *VED* generated on the film/substrate) correlation, persist (Zhao et al., 2023).

This thematic research-prospectus highlights the use of low-carbon steel substrates with Stellite 6-WC18 and WC19 as a coat-powder, irradiated by laser directed energy deposition (L-DED). These presented (or not) surface improvements, due to some conditions, according to Bartkowski et al. (2018). A higher concentration of WC-6 improved the substrate microhardness but weakened its corrosion resistance. Likewise, the laser beam power increase produced a WC concentration, also reducing the substrate hardness. In the ambit of Ti-6Al-4V alloy coated with WC's coat-powder, Li et al. (2020) highlight the coating surface defects, due to the high difference between the materials' thermal coefficients, using L-DED as a coating method. With this, Figueira et al. (2022) point to the L-PBF method as a solution (unlike the L-DED method), due to the possibility of a lower coating heat interaction, and employment due to more controlled *VED*. For L-PBF, in an additional way, Weng et al. (2014) explain that the coating should be carried out by irradiation of a thin layer or film (with or not a subsequent multilayer). With an initial low-P laser passing (or high v_s) ensuring a powder pre-sintering, followed by another passing with high-P (or low v_s) for powder fusion on the substrate. But, in order to do this, the coat-powder particles must be reduced for the asperging process, add Volu et al. (2023) add. To ensure the powder-bed uniformity distribution at the substrate surface and facilitate this process. At last, Teleginski (2016) concluded that these factors group still needs to be analyzed by grouping, without considering it as a single possibility.

This overview shows that both WC properties and laser parameters influence the behavior of the coated part. As a result, a research opportunity arises, since there are still scenarios to be investigated in the field of aeronautical materials (Volu et al., 2023). Therefore, this paper aimed to evaluate the chemical and mechanical properties of Ti-6Al-4V samples coated with WC-Co coat-powder deposited by L-PBF. To verify the correlation of laser parameters and coating properties, using a 70W CO_2 laser, by analysis of initial and coated samples by optical and scanning electron microscopy (OM, SEM), X-ray diffraction (XRD), energy dispersive spectroscopy (EDS), Vickers microhardness (MHV), and wear resistance test (WRT).

1 EXPERIMENTAL PROCEDURES

The experimental development was segmented by three steps: analysis of the starting materials, sample preparation, and analysis of the coated samples. Firstly, starting substrates and coating powder were characterized. Next, these were prepared and characterized again. Sequentially, the L-PBF deposition was carried out. Initially, an aqueous suspension containing coating powder was asperged on prepared substrates, and this thickness was measured, followed by the laser irradiation. Finally, the coated samples were evaluated, as Figure 1’s flowchart shows.

Figure 1 - Experimental development steps flowchart

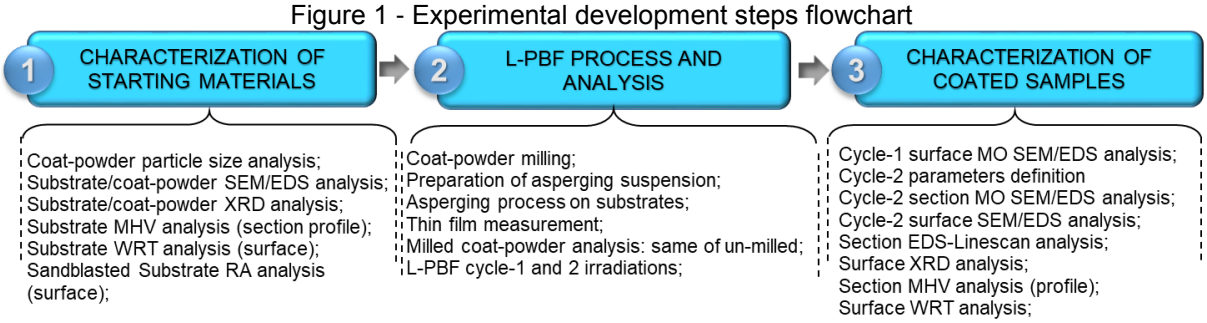

Source: Authors (2025).

1.1 STARTING MATERIALS PREPARATION AND ANALYSIS

For substrate material, a hot-rolled and annealed (750 °C/2 h) Ti-6Al-4V alloy. The original cylindrical dowel (1 m in length and 24.4 mm in diameter) was sliced into 3 mm thick discs using a laboratory saw. Next, the discs were sandblasted to improve coat adhesion using a blast chamber. This procedure was carried out, taking into account previous results (Volu et al., 2023). That showed a significant improvement in the coating anchorage, by the surface of substrate's roughness index (RA), considering the L-PBF method for deposition. Then, the starting discs were ultrasonically bathed (for 30 min and 20 kHz) in acetone.

As a coating, a commercial WC-Co-Cr coat-powder (here named as 'W_c'), with properties shown in Table 1 (according to the supplier). For film deposition by asperging, for L-PBF, the W_c particles were size reduced in order to facilitate the passage of coat-powder through the asperging nozzle gun. To this end, a mixture of 100 ml ethyl alcohol and WC-Co-Cr was ground into a ball-mill for 60 min and 500 rpm, using 5 tungsten carbide balls (with 30 mm diameter). The ground mixture was dried in an oven for 24 h at 60°C, obtaining the milled powder (here named as 'W_m').

Table 1- W_c coat-powder Properties, according to the supplier.

Material Properties				
Compounds:	**WC**	**Co**	**Cr**	**WC-Co-Cr**
Molecular proportion '*p*' (Weight% %)	**84**	**10**	**6**	**100**
Specific mass 'ρ' (kg/m³)	**0.156**	**0.0089**	**0.0072**	**0.0146**
Thermal conductivity '*K*' (W/cm.K)	**58**	**96**	**89**	**63**
Thermal diffusivity '*k*' (cm²/s)	**0.02**	**0.03**	**0.03**	**0.03**
Reflectivity '*R*' (T^{-1})	**-**	**-**	**-**	**0**
Fusion temperature '$T°_{(z,\,t)}$' (K)	**-**	**-**	**-**	**3160**

Source: WC supplier, adapted by the Authors (2025).

1.2 SAMPLE PREPARATION WITH L-PBF PROCESS BY CO_2 LASER

Before and after this preparation, the materials were characterized according to the analyses shown in Figure 1. For this purpose, certain preparations, parameters, and methodologies were applied in the same way in all the experimental steps (according to Figure 1) for analyzing the samples, as shown in Table 2.

Table 2- Procedures for all sample analysis.

Characterization	Parameters	Preparation	Method
MO and SEM/EDS	Various magnifications and different energies as well in detail throughout the paper	Bakelite embedding -> sanding sequence: 220, 400, and 1200 grits -> polishing alumina of 1 and 0.3 μm grits -> Kroll reagent	None specific
Particle size	Average obtained from a triplicate of 10 runs	None	Laser diffraction
Roughness (RA)	Step: 0.1 um, length: 1.1 mm, and tip deep: 0.01mm	Sandblasting	Surface tip run
XRD	Step: 0.02°, 2θ: 20°-90° and time step: 10 s	Surface sanding (600 grit)	X-ray at 45 kV/40 mA
MHV	Load: 25 Mn and time: 10 s	Same as MO and SEM/EDS characterization	Berkovich indenter
WRT	Load: 3 N, speed: 10 cm/s, distance: 50 mm, and track length: 4 mm	Sandblasting (uncoated samples), none for coated ones	Pin on disc: 3mm spherical tip

Source: Authors (2025).

After grinding, W_m was also characterized (according to Figure 1). Next, for L-PBF deposition, a W_m thin film was deposited on sandblasted Ti-alloy disc surfaces. To this end, a mixture of W_m (50 g) and ethyl alcohol (300 ml) was asperged on the surface discs, using a pneumatic gun (3 Bar, without any air treatment). Then, residual alcohol was dried for 1 hour at 60°C in the oven, as Figure 2 shows.

Figure 2 - Asperging process for Wm film deposition under starting Ti alloy discs.

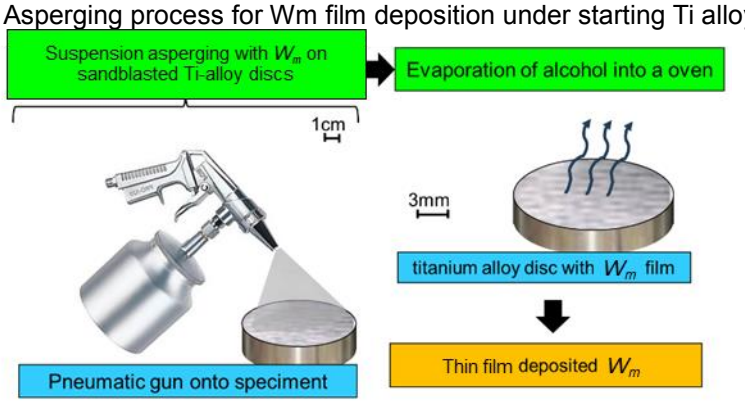

Source: Authors (2025).

Sequentially, L-PBF was carried out using a Gaussian profile CO_2 laser beam. This operates with a continuous wavelength at a 'λ' of 10.6 μm, 70 W of maximum 'P', and a b_d = 180 μm. The apparatus is fixed over a platform, with the laser headstock performing the beam control (x-y-axis for coat-path performing), with a pre-defined 'v_s' by the comp interface. In addition, to minimize oxidation, argon gas was used as a shielding, with a 's_g' flow of 5 L/min. Figure 3 details this L-PBF set-up apparatus.

Figure 3 – Schematic diagram of the laser beam apparatus layout.

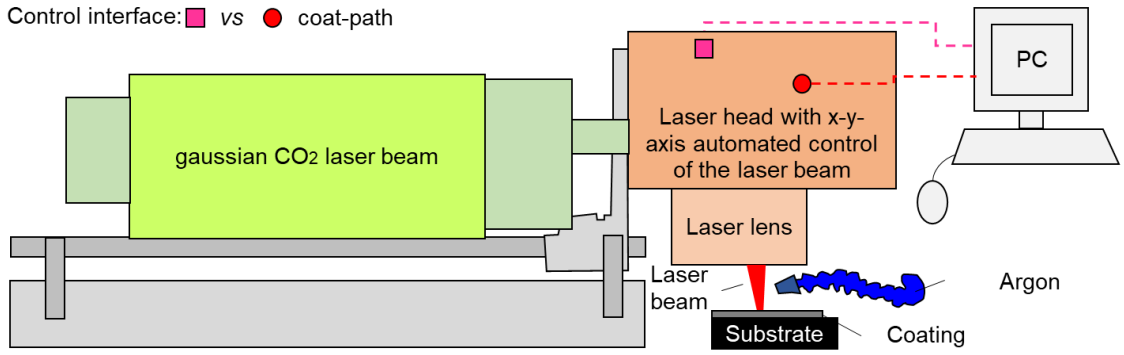

Source: Authors (2025).

Concomitantly, the irradiation was carried out in two steps: cycle-1 and cycle-2. The first aimed at the v_s parameter determination, starting from different v_s. With the laser headstock performing a coat-path composed of 137 track lines of length '*y*' of 17.3 mm with an overlapping between lines 'O_v' of 70%, i.e., with a 126 µm distance between each track-line, assuming a track width '*W*' equal to b_d. This produces a coat area corresponding to one square circumscribed on Ti-alloy disks. Next, these coated samples were analyzed for cycle-2 parameters definition

For cycle-1 parameters definition, were considered film thickness 'T_k', materials properties, and literature were considered. With this, T_k (in cm) and coat-powder properties are inserted into Duley's (1976) Equation 1, estimating v_s, considering an inverse proportionality between v_s and materials melting, according to Chagas (2016).

$$T°(T_k, t) = \frac{2(1-R)I_0}{K}\left[\sqrt{k.t}\right].\left[\frac{z}{2\sqrt{T_k.t}}\right].\left[\frac{2}{\sqrt{\pi}}\right].\int_x^{\infty}\int_x^{\infty} e^{-y^2}.dy;\ I_0 = \frac{2P}{\pi(0.5b_d)^2}\ ;t \qquad (1)$$

Where 'I_0' laser intensity (W/cm²), '*t*' laser passing interaction time (s) as a function of *y* (mm). Thus, considering these assertions was determined a 10-100 mm/s range of v_s was determined for cycle-1, a total of 8 v_s experiments, as Table 3 shows; also presenting the number of layers for growth 'N_c' (T^{-1}) for L-PBF's film deposition.

Table 3 - Parameters adopted for cycle-1.

Parameters	Values
Power '*P*' (W)	**70**
Beam diameter 'b_d' (µm)	**180**
Overlay tracks '*Ov*' (%)	**70**
Film thickness 'T_k' (cm)	**~4.10^{-4}**
Number of coating layers 'N_c' (T^{-1})	**1**
Laser velocity of scanning 'v_s' (mm/s)	**10 20 30 40 50 60 80 100**

Source: Authors (2025).

In addition, for the cycle-1 definition, consider other specifications according to Santos's (2014) previous studies. In addition, other previous studies (Teixeira, 2016; Silva et al., 2024) also contributed to the definition of the cycle-1 parameters. On this issue, one of the deciding factors was the *P* parameter of 70 W. Likewise, the optimum b_d = 180 µm; in the focal region, between lens and film, also proved to be satisfactory. Similarly, the O_v of 70% showed the best results for the CO_2 laser.

Therefore, for this paper's experiment, the P and b_d variations don't show pertinence. As a result, v_s was the only parameter to be varied for the cycle-1 experiment.

With this in mind, the 8 coat-areas were produced with one-layer and 137 tracks, highlighting 9 tracks in Figure 4[A] scheme. Thus, based on cycle-1 analysis for homogeneity, presence of flaws, and composition (by Figure's analysis), cycle-2 parameters were determined, according to Table 4. Nevertheless, for cycle-2, 3 layers of growth (N_c = 3). With this, the film asperging (similarly to cycle-1) was repeated before each new irradiation. With the line's coat-path direction alternating by 90º under the last track-line of the previous layer, as Figure 4[B] illustrates.

Figure 4 – Scheme of L-PBF process: [A] cycle-1 execution and O_v detail and [B] cycle-2 execution.

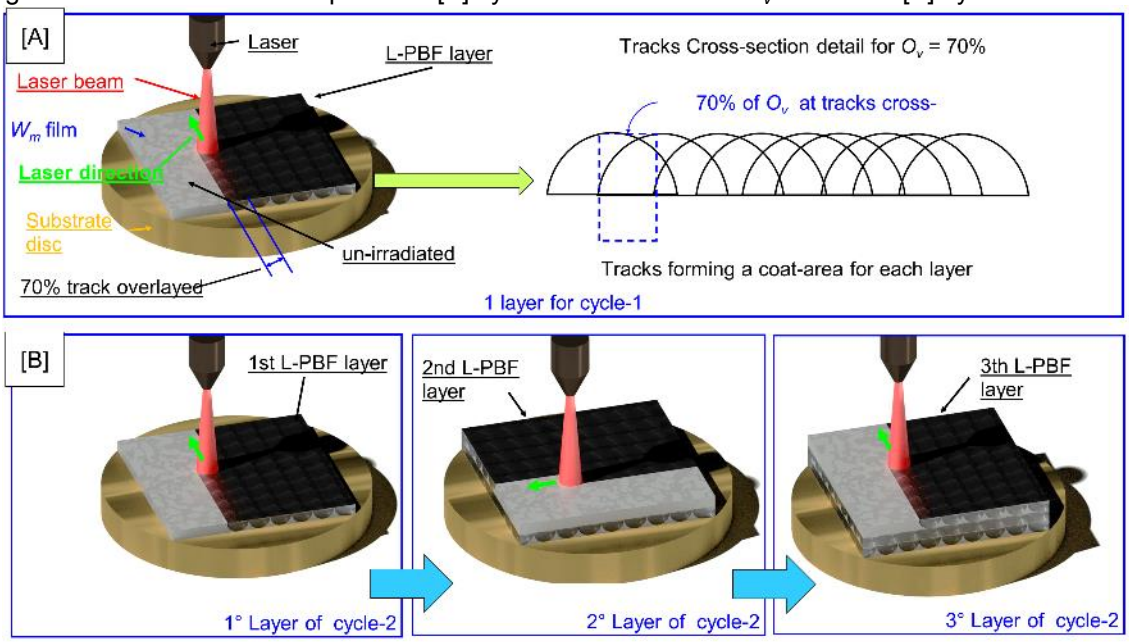

Source: Authors (2025).

Table 4 - Parameters adopted for cycle-2.

Power P W	Beam diameter b_d µm	Overlay tracks O_v %	Thickness T_k µm	Laser velocity of scanning v_s mm/s	Number of coating layers N_c T^{-1}
70	**180**	**70**	**~40**	**30**	**3**

Source: Authors (2025).

2.3 THIN FILM THICKNESS MEASUREMENT AND COATED SAMPLES ANALYSES

Before the L-PBF irradiation process in cycle 1, T_k was measured. For this purpose, the 'scratching' technique, recommended by Jardim (2020) and Volu et al. (2023), was performed on cycle-1's asperged film surface. This consists of a fixed blade with a known angle triangular tip (52.13°); scraping the film surface, with subsequent OM scratch analysis. The sample with the film was attached to the analyzer of a nano-identifier equipped with a computer numerical control (CNC) triaxial control system. Then, the blade was attached to the equipment's indentation arm, with the tip down and positioned normally to the surface of the film. Then, the blade performed the surface scratch on the film (with a load of 5 N). This movement took place in the direction normal to the blade surface with a speed of 0.1 mm/s, as

shown in Figure 5[A]. The scratch was then OM analyzed to estimate T_k thickness. For this purpose, the measurements obtained from the surface micrographs were inserted into Equation 2 trigonometric relationship. Where, 'α_b' is the blade angle (degrees), 's_w' and 'b_w' are the surface (Figure 5[B]) and bottom (Figure 5[C]) scratch widths (considering that this method takes the average between measurements, with this, erroneous measurements may appear due to the size of the target, but in general, the method is efficient for a quick measurement). These measures were obtained (triplicate) by edges focusing on OM. Parallelly, the apparent specific gravity of powder-bed 'ρ_a' was determined by weighing before and after the aspersion process.

$$T_k \quad [s_w - b_w] \quad [\quad (\propto_b)]^{-1} \tag{2}$$

Figure 5 – Scheme of T_k measurement: [A] tip micrograph and set-up, [B] OM of top and [C] bottom.

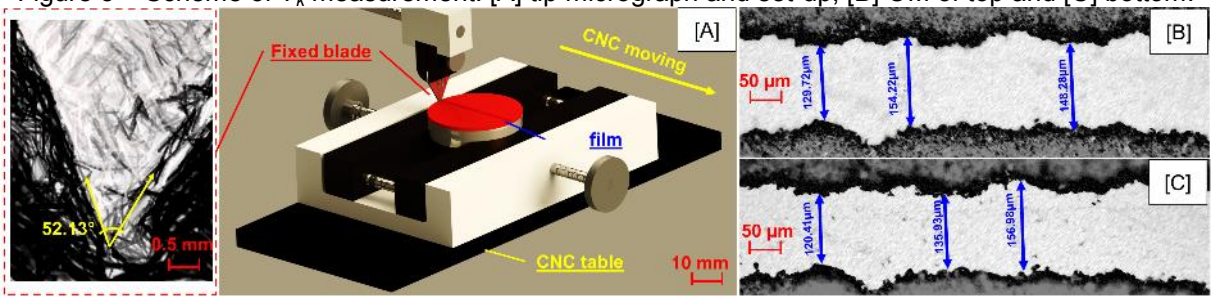

Source: Authors (2025).

After obtaining *Tk*, cycle-1 and cycle-2 L-PBF, the cycle-1 surfaces and cycle-2 surfaces, and sections were analyzed according to Figure 1 and Table 2. In addition, during the coated samples' MO and SEM analysis, dilution '*D*' morphological aspects were also evaluated, according to Goodarzi et al. (2015), Equation 3 and Figure 6, as well as aspects of *VED*, according to Equation 4.

$$D = \frac{A_c}{A_m + A_c} \tag{3}$$

$$VED \quad - \quad \frac{P}{} \tag{4}$$

Figure 6 - Schematic representation of coat dilution.

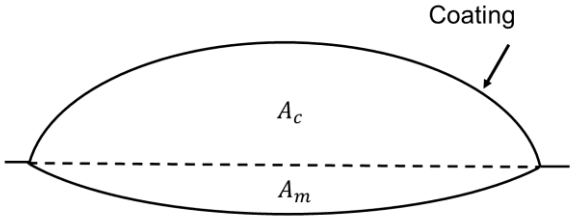

Substrate

Source: Adapted from Goodarzi et al. (2015).

Where *D* is the coat dilution (%); 'A_c' is the coat area (mm²); and '*Am*' is the melting interface area (mm²). Noting that A_c and A_m, as well as the HAZ area 'A_{HAZ}' (in mm²) from the L-PBF process, were measured by the process of rasterizing the micrographs with the spline tool in the Inventory software.

In a complementary way, W_m and cycle-2 samples crystalline phases were evaluated in the light of the WC-Co-Cr thermic decomposition process, described by Vinayo et al. (1985), Equation 5. This procedure, in view of the WC-Co-Cr transformation, was taken due to the known penetration limitation of the XRD test, according to Krawitz's (1985) statements.

$$\begin{aligned} &2WC \xrightarrow{\Delta} W_2C + C \\ &W_2C + \frac{1}{2}O_2 \xrightarrow{\Delta} W_2(C,O) \\ &W_2(C,O) \xrightarrow{\Delta} 2W + CO \end{aligned} \tag{5}$$

Finally, destructive mechanical tests; according to Figure 1 and Table 2, of initial and cycle-2 samples were analyzed in view of volumetric loosing material comparison (for WRT) and hardness increasing (or not) observations (for MHV tests) at the section hardness profiles.

Thus, this 3-step methodology aimed to compare, in terms of WRT and MHV, Ti alloys coated or not with WC-Co-Cr, by the aspersion process and L-PBF irradiation. Similarly, the reduced (W_m) and in natura (W_c) coat-powder was also compared to see if any significant differences could influence the coat morphology. As well as its A_{HAZ} and *VED* relationship, the microstructure and RA of the substrate surface are considered. The flowchart in Figure 7 summarizes this experiment.

Figure 7 - Flowchart summarizing the experimental procedures.

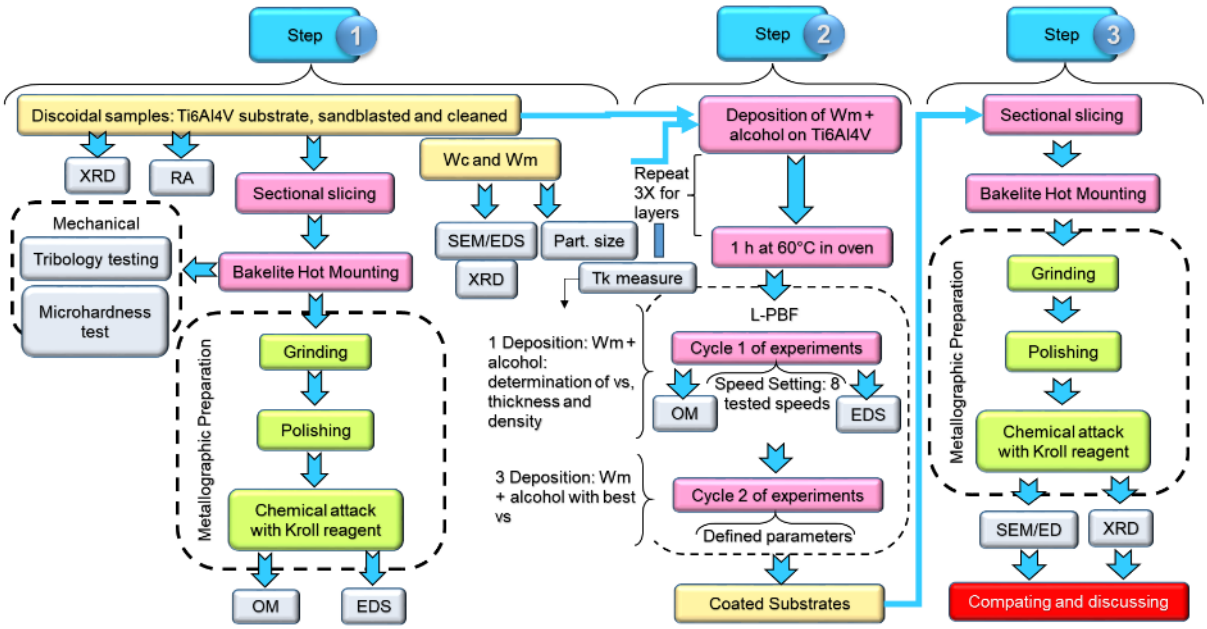

Source: Authors (2025).

3 RESULTS AND DISCUSSIONS

The microstructure and crystalline phases properties of Ti-6Al-4V, W_c, and W_m were evaluated regarding the alloy characteristics and improvements from the powder milling process. Likewise, microstructural, chemical, and mechanical properties were compared between starting titanium discs and the cycle-2 sample, in the spectrum of wear resistance gains; also, they were evaluated through *D*, *VED,* and quality of coating.

3.1 WC COAT-POWDER AND TITANIUM STARTING DISC PROPERTIES

The W_c and W_m particle sizes showed a discrepancy between them, as Figure 8[A] graph shows. This result was to be expected, according to previous studies (Volu et al., 2023; Silva et al., 2024). Where the maximum particle size was 43 µm for 4 µm, facilitating the aspersing process. Nevertheless, the milling transformed predominantly rounded to angular particles, as Figure 8[B] SEM micrographs. The powder's crystallography and EDS, on the other hand, remained within the typical values; according to Kim, Rohrer (2004) and Ulusoy (2023), as presented by Figures 8[C], 8[D] and Table 5. Where the predominance of WC and W_2C was confirmed, presenting also the intermediate Co_3W_3C phase, with low predominance. Li et al. (2020) point out that the presence of Co_3W_3C is detrimental for coating, occurring regularly in commercial WC-Co-Cr coat-powders (Volu et al., 2023), due to its more fragile structure. Where, during the sintering process, an intermediate phase is formed due to WC dissolution and carbon losses (Bartkowski et al., 2018; Marques et al., 2013). With this, the lower proportionality, as observed in XRD of Figure 8[C] and EDS (Table 5), doesn't affect the coat quality.

Ti-6Al-4V alloy, in turn, presented a typical composition (Makurat-Kasprolewicz & Ossowska, 2023; Rominiyi & Mashinini, 2024) and, within the ASTM F13635 (American Society for Testing & Materials [ASTM], 2014) criteria, is also presented in Table 3. With a microstructure composed of equiaxial grains, as the OM micrography of Figure 8[E] shows. In this context, Rominiyi and Mashinini (2024) state that the annealing after rolling attributes an equiaxial grain predominance, implying its high ductility and high fatigue resistance. However, it presents lower fracture toughness and creep resistance compared to lamellar grain microstructures. The crystalline phases, on the other hand, showed an α-Ti and β-Ti predominance, as Figure 6[F] graph, being an expected crystallography for aeronautics titanium alloys (Moskalewicz et al., 2010; Makurat-Kasprolewicz & Ossowska, 2023; Rominiyi & Mashinini, 2024).

Likewise, the Ti-alloy also presented a satisfactory RA, according to previous studies and literature, which determined a good anchoring of the WC with this RA index of 1.02 µm; to improve the coat-coupling (Jeyaprakash et al., 2019; Volu et al., 2023; Silva et al., 2024), as Figure 6[F] shows.

Figure 8 - Materials properties: [A] W_m and W_c granulometry, [B, C] W_c and W_m SEM, [D] W_m and W_c XRD, [E] Ti-6Al-4V OM, [F] Ti-6Al-4V XRD, and [G] Ti-6Al-4V RA.

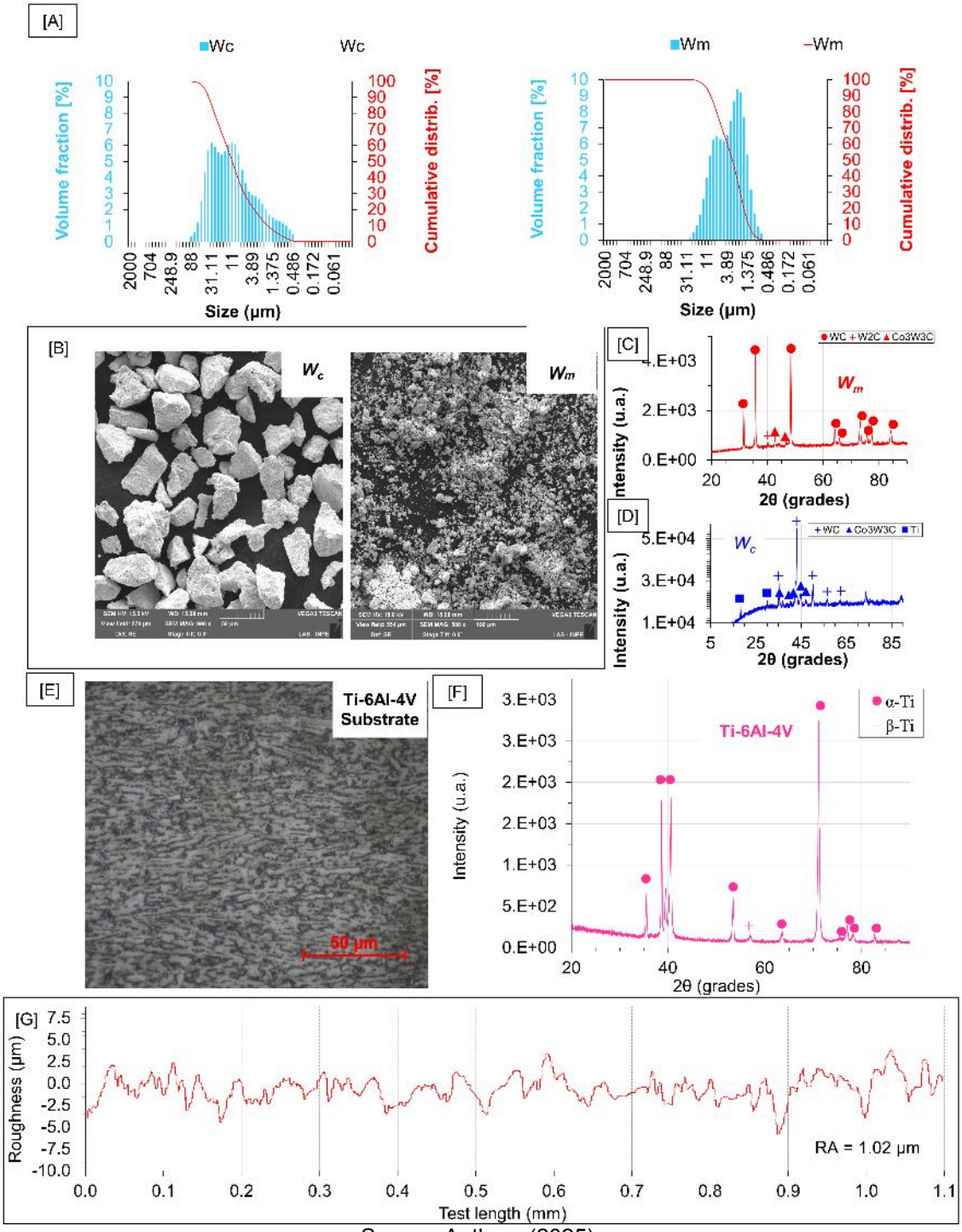

Source: Authors (2025).

Table 5 - Chemical composition of starting materials, substrate, and coat-powders.

Element	Element		Al	V	Fe	O	C	Co	Cr	Ti	W	Others
Ti-6Al-4V	**Criteria**	**Wt%**	**6.05**	**4.16**	**0.17**	**0.1**	**0.03**	**-**	**-**	**Bal.**	**-**	**-**
	Sample	**Wt%**	**6.00**	**3.10**	**-**	**-**	**-**	**-**	**-**	**90.1**	**-**	**-**
WC-Co-Cr	***W_c***	**Wt%**	**-**	**-**	**-**	**-**	**5-6**	**9-11**	**4-5**	**-**	**Bal.**	**≤ 1**
	W_m	**Wt%**	**-**	**-**	**-**	**-**	**8.8**	**9.6**	**3.9**	**-**	**78**	**-**

Source: Authors (2025).

3.2. FILM AND CYCLE-1 SAMPLES PROPERTIES

As previously presented, the average-T_k was estimated in ~40 ± 11 µm. With average values of: s_w = 154.22 µm and b_w = 120.47 µm. The apparent density 'ρ_a', on the other hand, was estimated in 7.66 ± 0.27 g/cm³, or 50% of the real density 'ρ_r' of Ti-alloy of ~14.6 g/cm³, according to Callister Jr. and Rethwisch (2014). The irradiated surfaces, according to cycle-1 parameters, presented surface micrographs (OM) and elemental composition (EDS) as Figure 9.

According to these results, it was concluded that the v_s plays the main role in the coat effectiveness. Where, a low v_s; such as 10 and 20 mm/s; there was a complete vaporization and high levels of substrate surface oxidation. Being confirmed by high levels of yellow-coloured oxides from OM. In addition, these v_s presented low WC concentrations (by weight percentage W%), from the EDS graph. Otherwise, high v_s such as 40-100 mm/s haven't provided satisfactory energy to melt the W_m metal matrix. Being verified by large flaws regions, evidenced by an occurrence of 'balling' on the surface. In addition, these high v_s presented low deposition rates, identified by low levels of WC and other typically found elements (by EDS).

Figure 9 - Microstructures by OM and EDS of coated samples with cycle-1 parameters.

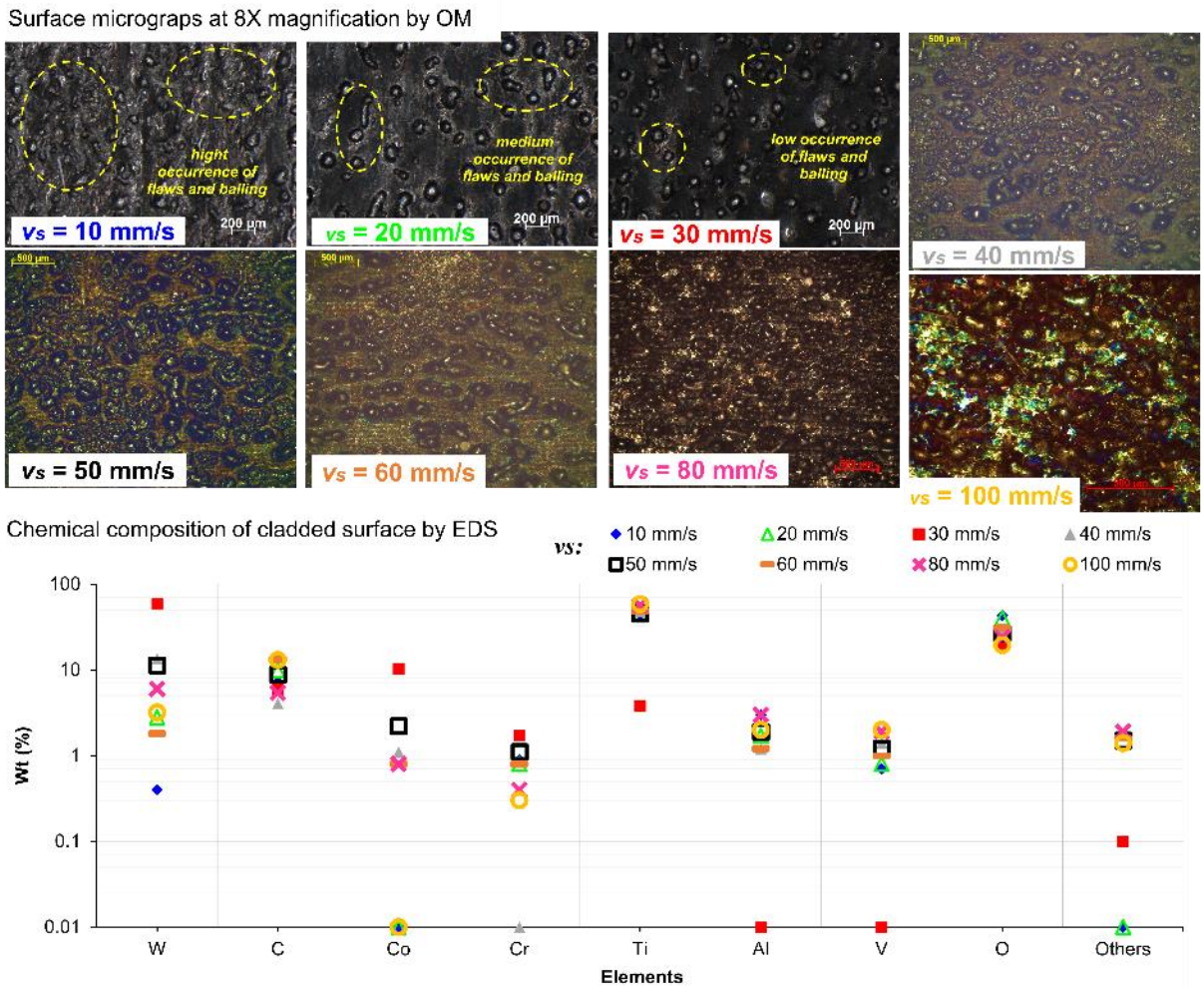

Source: Authors (2025).

In the context of densification, Teixeira (2016) explains that high v_s promotes an irradiation energy (I_e) sufficient for film heating, without significantly layer thickening. Obtaining a density of the irradiated film ' $i\rho_a$ ' lower than ρ_r, i.e., '$i\rho_a$' < ρ_r. Low v_s, on the other hand, promotes so high Ie, which causes, since coating mass loss, by vaporization and molten material spatter, to its total vaporization. Therefore, as Chagas (2016) explains, the v_s should be limited between material fusion and diffusion with substrate points, ensuring a satisfactory layer densification, i.e., $i\rho_a \sim \rho_r$. Thus, as presented by Table 4, the v_s = 30 mm/s presented the most satisfactory middle ground, in view of the OM and EDS, as well as to predict a final densification process about $i\rho_a \sim \rho_r$.

3.3. CYCLE-2 SAMPLE PROPERTIES

The cycle-2 sample XRD, to the depth of 5 µm, shows a predominance of W and W_2C crystalline phases, as the diffractogram of Figure 10 shows. With this, the superficial decomposition of a WC portion was confirmed, according to Vinayo et al. (1985), Equation 5. Nevertheless, it may contain greater quantities of the WC phase inside the coating. With this, as Krawitz (1985) stated, this is an inconclusive analysis for deeper layers.

Figure 10 - XRD diffractogram of cycle-2 sample.

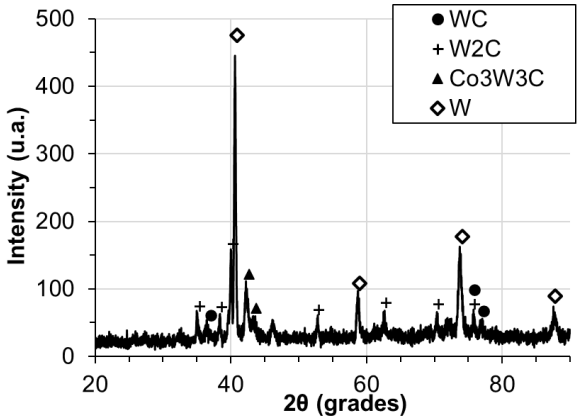

Source: Authors (2025).

Likewise, oxidation of the surface, despite the argon flux during L-PBF. Consequently, contributing to corrosion and its detachment, as evidenced by SEM micrographs of Figure 11[A]. Moreover, the EDS mapping shows agglomerates of WC. With this, the L-PBF process left some substrate parts exposed, as presented by Figure 11[B], with contours between agglomerates indicating titanium, aluminum, and vanadium. While the coalesced particles indicate tungsten, cobalt, and chromium presence. Oxygen is virtually found in the entire region, indicating the oxidation of both coat and substrate.

In this context, as Wang et al. (2013) highlighted, the cracks are a consequence of high thermal gradients and physical-thermal differences between ceramic materials and metallic substrates. Being a ceramic-coating intrinsic problem, and recurrently observed. Where the multilayer of L-PBF deposition facilitates these defects, due to the superposition and residual stress effects. Nonetheless, according to Zhao et al. (2015), these can be mitigated with different composition multilayer applications, allowing a smoothed transition. However, the cycle-2 coating improved

the global properties of the starting material, despite the surface defects observed, as will be seen later in this article.

Figure 11 - Microstructures of cycle-2 sample surface: [A] by SEM and [B] by EDS mapping.

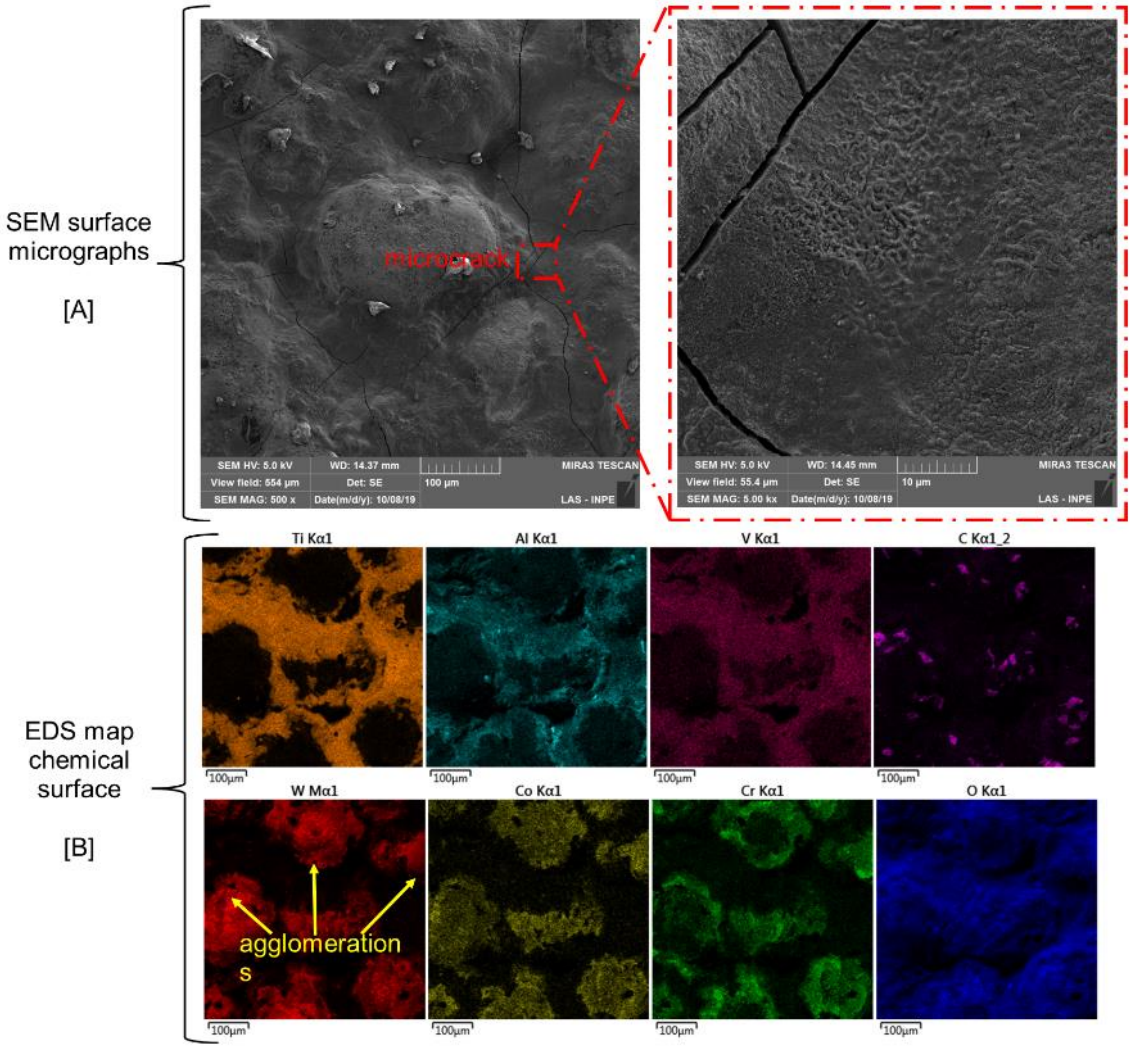

Source: Authors (2025).

The first evidence of this improvement can be seen in the morphological characteristics. In addition to the relationship between *VED* and A_{HAZ}. In this sense, the OM of the cycle-2 sample cross-section revealed a microstructure with high-layer-densification, as presented by Figure 12[A] (this image highlights the coat of the region through the focus adjustment of the microscope). With a D ~ 15 %, obtained from Equation 3 (and spline method), within the range recommended by Goodarzi et al. (2015). According to the authors, a high *D* impairs the coating's mechanical and corrosive properties. Otherwise, a *D* < 5% doesn't ensure a coat anchoring by metallurgical bonding (with balling formation). Where a value of 5-15 % is the most appropriate for a well-coating morphology. In addition, the micrograph, with spline method application, shows an average coating thickness 'T_c' of 60 ± 9 µm for 3 layers. In other words, an average thickness for each layer of 20 µm. This confirms the assumption of using a v_s = 30 mm/s. In addition to conforming to the assertions of Teixeira (2016) for densification of $i\rho_a \sim \rho_r$ or 11.49 ± 0.27 g/cm³ ~ 14.6 g/cm³.

Furthermore, macro-pores and perpendicular cracks, throughout the coating cross-section. According to Chagas (2016), the presence of pores occurs due to the

gases trapped from the WC decomposition and rapid matrix solidification. The cracks, on the other hand, occur analogously to the surface defects highlighted by Moskalewicz et al. (2010) and Zhao et al. (2015). Despite this, an efficient use of I_e was determined by A_{HAZ} and *VED* correlating. Where the *VED* = 46.3 ± 0.29 J/mm³ remains within Figueira's et al. (2022) criteria (43-70 J/mm³), for a thin coating (15-30 µm) and an A_{HAZ} < HAZ-length. Assuming that the width of the HAZ for a single track its equal to *W* ($W = b_d$ = 180 µm) and a HAZ-length of 100 µm (by spline method), according Figure 3[B] (which highlights the HAZ of Figure[A] same region, through the other focus adjustment), for obtaining an A_{HAZ} = 0.018 ± 0.003 mm².

Likewise, Figure 12[B] shows a microstructural change to acicular grains, as a result of a martensitic transformation from the β-phase field (rapid cooling). Although this change generates crystal structure distortions on steel alloys, as pointed out by Makurat-Kasprolewicz and Ossowska (2023). Unlike these, this transformation in titanium alloys has a moderate effect and doesn't generate large crystalline distortions.

Figure 12 – Cycle-2 coat cross-section: [A] highlighting the coat and [B] highlighting the HAZ region.

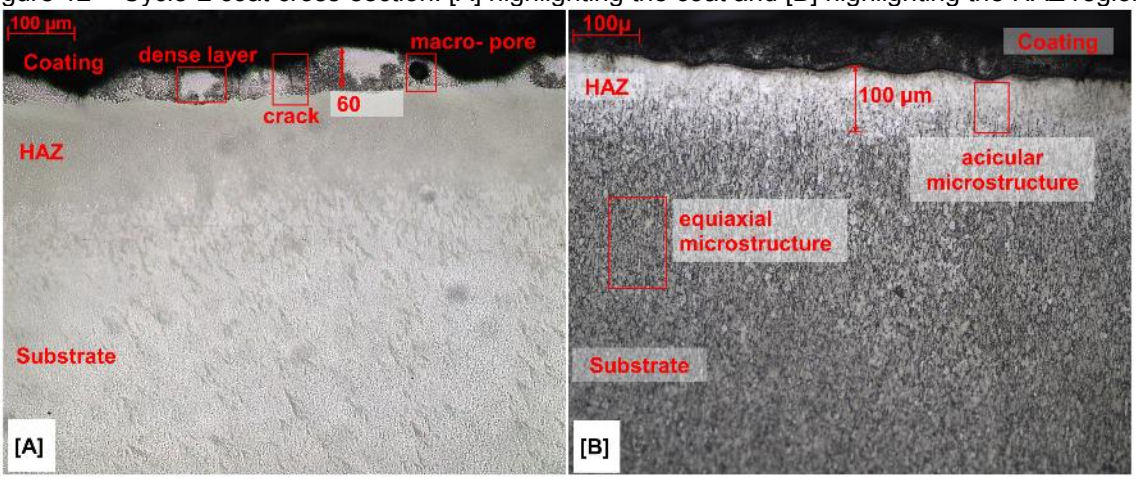

Source: Authors (2025).

The SEM of cross-section, on the other hand, shows a microstructure imbued with refined granulation, verifying a globular morphology with 1 µm average-sized grains, as Figure 13[A] shows. According to Makurat-Kasprolewicz and Ossowska (2023), finer-grained microstructures provide higher hardness and wear resistance. With this, a probable mechanical improvement for Ti-alloy could be observed. Furthermore, punctual EDS: EDS_1-EDS_7, from Figure 13[A], showed an elemental distribution with well-defined regions. With lighter coloration regions mainly formed by W and C (EDS_1 and EDS_5), the W migration (heavier element) occurs to the diffusion lower region (substrate and coating mixture zone). While the darker contours are mainly formed by Co and Cr, indicating the surrounding carbide particles, according to Table 4.

In this same analysis, the quantitative EDS mapping of Figure 13[B] showed the aluminum dispersion. With a lower concentration in the whole area, including the coating near the diffusion interface region. Indicating the migration of some portion from the substrate. As Upadhyaya (1999) stated, the aluminum acts as a tungsten carbide grain growth inhibitor. With this, the Al contributes to microstructure refinement, explaining the granular characteristics of the coating. Hence, the EDS line scan graph of Figure 14, evidenced more clearly this diffusional region, showing

a gradual mix of coating (W, C, Co, and Cr) and substrate (Ti, Al, and V) elements. Thus, highlighting the metallurgical bonding occurrence.

Figure 1SEM/EDS of cycle-2 sample: [A] SEM and EDS point analysis and [B] EDS mapping.

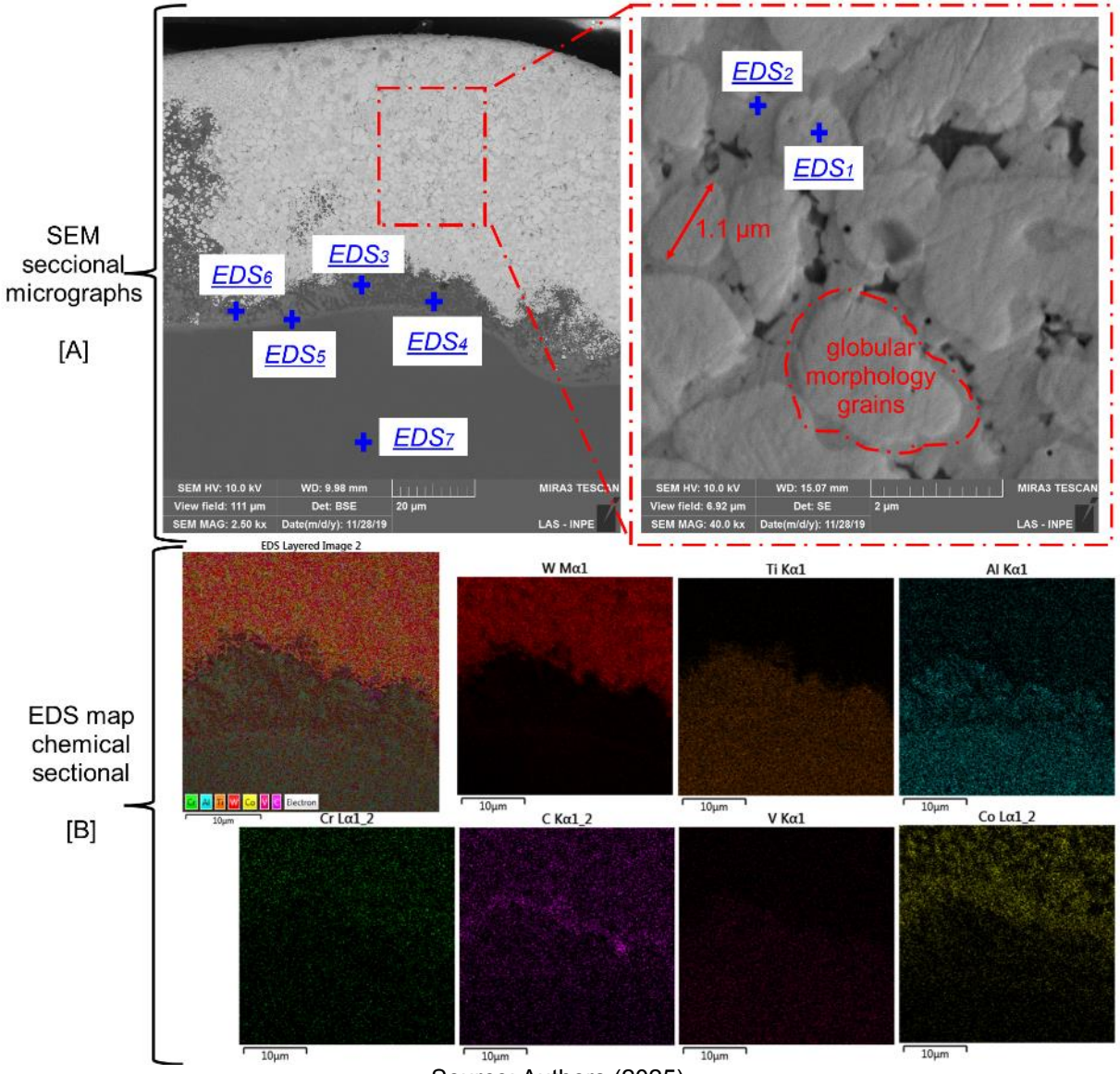

Source: Authors (2025).

Table 6 - EDS composition of EDS_1-EDS_7 points.

Regions:	Cladding		Diffusional interface (metallurgical bonding)				Substrate
Points:	EDS_1	EDS_2	EDS_3	EDS_4	EDS_5	EDS_6	EDS_7
Elements	Wt(%)	Wt(%)	Wt(%)	Wt(%)	Wt(%)	Wt(%)	Wt(%)
W	82.2	47.1	18.4	2.7	15.6	6.0	-
C	14.3	12.8	6.1	7.0	5.8	5.9	-
Co	1.7	32.5	6.3	1.1	4.4	-	-
Cr	1.8	7.5	2.0	-	1.2	0.3	-
Ti	-	-	57.9	78.5	62.1	74.9	90.9
Al	-	-	5.9	1.4	5.3	5.4	6.0
V	-	-	3.4	0.3	2.3	2.0	3.1
O	-	-	-	9.0	3.3	5.5	-

Source: Authors (2025).

Figure 2 - EDS line scan of coat sectional cut with cycle-2 parameters.

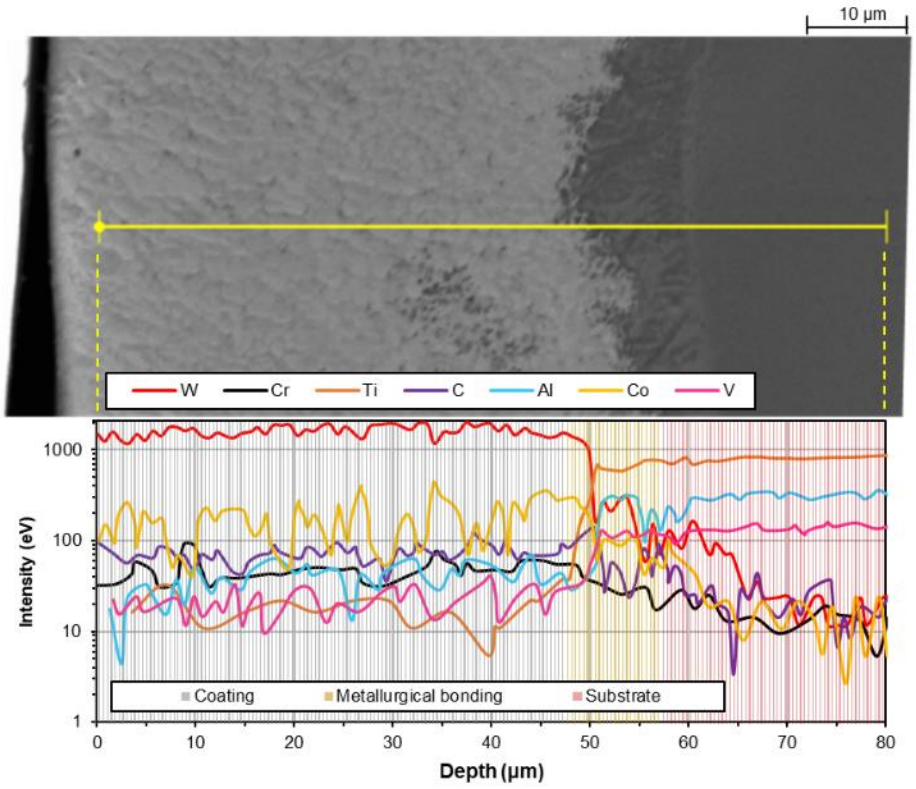

Source: Authors (2025).

3.3 MECHANICAL IMPROVEMENTS FROM CYCLE-2 PARAMETERS

Microstructural analysis indicated wear resistance improvements over starting Ti-alloy discs, by cycle-2 parameters. In this case, tribological tests confirmed this analysis, being the coating hardness has improved more than five times. With this, an average hardness of coated substrates of 25 GPa (2500 HV), against a hardness of starting samples of 4 GPa (400 HV), as shown in Figure 15. In addition, Figure 15[A] showed other comparatives, according literature (Bartkowski et al., 2018; Dhanda et al., 2014; Tijo & Masanta, 2017; Jeyaprakash et al., 2019). With the cross-section hardness profiling, as Figure 15[B] details, starting from 5 µm to 300 µm of substrate depth. With this, diffusion region measurements showed hardness above 10 GPA (1000 HV). Where a reduction in hardness typically occurs, due to coat elements. Likewise, HAZ region measurements revealed hardness around 5 GPa (500 HV). Also, high values are typically found in this region (Rominiyi & Mashinini, 2024).

Figure 3MHV test: [A] Compared to literature and [B] detailed profiling for cycle-2.

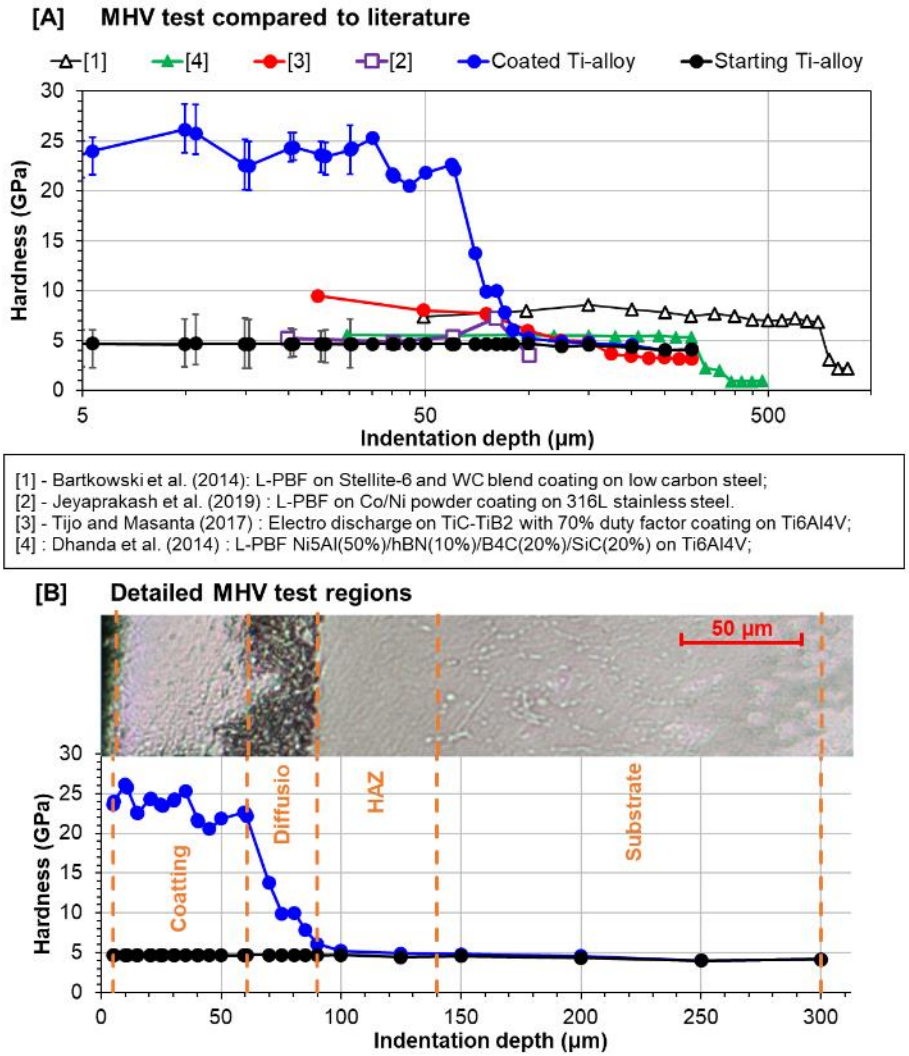

Source: Authors (2025).

As shown by Figure 15[A], the W_m coating has a higher hardness than literature coatings. Where the comparison was made with techniques of electro discharge for coating (Tijo & Masanta, 2017) and L-PBF (Bartkowski et al., 2018; Dhanda et al., 2014; Jeyaprakash et al., 2019). With other irradiation parameters and materials: Ni5Al(50%)/hBN(10%)/B4C(20%)/SiC(20%), Stellite-6, Co/Ni and WC.

According to Lassner and Schubert (1999), these values are slightly above the typical WC phase, probably associated with the W_2C harder phase presence, confirming the carbide decarburization occurrence. Furthermore, the pin-on-plate test showed a coat with volumetric losses ~ 100 times lower than the starting Ti-alloy. In other words, a loss of $1.2x10^{-5}$ mm³/N.m (coated), against a loss of $1.4x10^{-3}$ mm³/N (uncoated), according Figure 16[A]. Similarly, the coating obtained an average friction coefficient '$f_{average}$' 65% times lower than the Ti-alloy substrate; i.e., 0.19 (T^{-1}) versus 0.55 (T^{-1}). Obtained from test curve stabilization '*f*', as shown by Figure 16[B]. Other results from literature (Moskalewicz et al., 2010; Lin & Lin, 2011; Guo et al., 2012; Dhanda et al., 2014; Amanov & Pyun, 2017; Tijo & Masanta, 2017) were also plotted for comparison.

Figure 16 - Friction properties of coated samples by cycle-2: [A] wear rate and [B] friction.

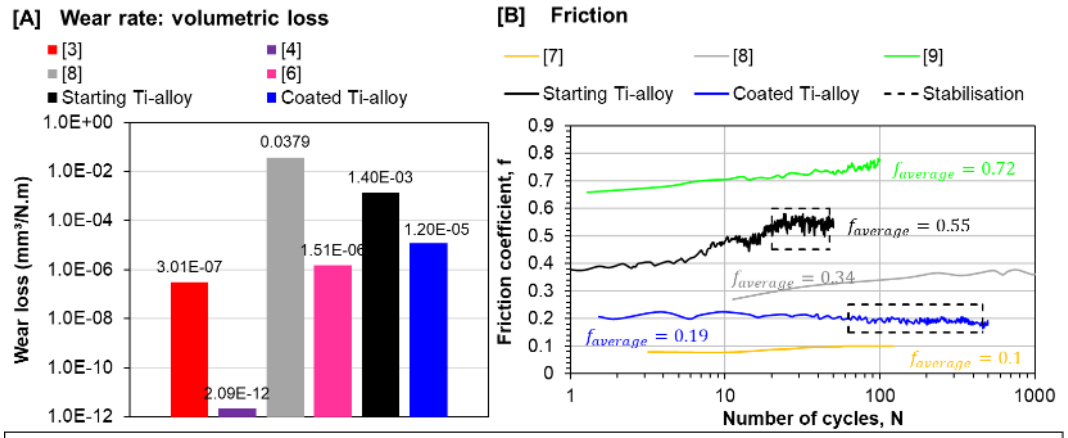

[6] - Guo et al. (2012): L-PBF of NiCrBSi/WC-Ni(50%) on Stainless steel Cr18Ni9Ti substrate;
[7] - Moskalewicz et al. (2010): Magnetron sputtered with nc-WC/a-C deposition on oxygen hardened Ti–6Al–4V substrate;
[8] - Lin and Lin (2011): Gas tungsten arc welding on Ti6Al4V with SiC coating;
[9] - Amanov and Pyun (2017): Ti6Al4V alloy surface nanocrystal by ultrasonic deposition.

Source: Authors (2025).

Figure 16[B] shows that the W_m coating surface, with cycle-2 parameters, had a lower $f_{average}$ than most of the studies presented. While in [A], the wear rate presents a loss similar to the literature. In this context, weld, laser, and vapor deposition coatings present higher wear resistance. In relation to ultrasonic surface deposition techniques. Likewise, the use of WC as a coating material presents the best improvements, in relation to the silicates, considering its use as a deposited powder cladding or associated with other matrices. With this, it is observed that the L-PBF, using a CO_2 laser, with WC coating brings an advantage to titanium alloys, on other coating techniques and materials. With this, the L-PBF method applied with WC-Co-Cr as a coating brings significant improvements to aeronautics titanium alloys in the environmental context of high physical stress and thermal variation that these parts are normally subjected. Thus, expanding its aeronautical use.

4 CONCLUSION

In this paper, physical, chemical, and tribological properties of titanium alloy starting samples coated with Wm by L-PBF (laser CO_2) were evaluated. The results showed improvements in wear resistance and hardness. During and after experimental procedures, some conclusions could be pointed out. Addressing the relationship between beam parameters and cladding quality.

The laser beam characteristics allowed a narrow working range for the cycle-2 coating process: P = 70 W, O_v = 70% and v_s = 30 mm/s. In which, even so, some sections of coating contain macro pores and surface cracks. With this, it can be concluded that the vs parameters can still be modified. To seek a superior quality for the cladding. In this same context, the coating cross-section still presented dense regions. In addition, a good anchorage between the WC/substrate is required. Likewise, this cross-section presented a microstructure imbued with refined grains with globular morphology and D~15%, being considered satisfactory. With this, the coating/substrate interface presents metallurgical bonding, due to the perception of a diffusional region containing elements of the coating and substrate. Concluding that cycle-2 parameters and PBF execution compensated for the WC sphericity loss due to the powder milling process.

Finally, wear resistance improvements were observed. With a hardness increase reaching 2500 HV, against 400 HV. Besides, an average hardness; considered a little accentuated in the HAZ and diffusion region of 1000 HV and 500 HV, respectively. In addition, the cladding surface obtained a 100-fold reduction in wear loss rate and a 65% reduction in f; compared to the starting titanium alloy. Concluding that this technique brought a significant improvement to titanium alloys. Considering the deficiencies and its application requirements in the aeronautical industry.

5 FUTURE SCOPE

In view of the presented conclusions, some research opportunities were highlighted, expanding this research theme. To complement these studies, carried out in the present paper, were made:

- Perform the bed-powder deposition together with the laser irradiation process, aiming to reduce oxidation, since the shielding gas flow wouldn't limit itself to avoid powder dispersion;
- Investigate other laser scan speeds ranges close to v_s = 30 mm/s, reducing the cladding temperatures to minimization of the decarburization effect;
- Perform a chemical gradient chemical of multilayer deposition, smoothing the transition of thermal properties between substrate and coating, thus reducing the formation.

ACKNOWLEDGEMENTS

The authors thank the capital and funding resources provided by the Pro-Defesa V Project (Case Number: 88887.961510/2024-00). Special thanks for the Instituto de Estudos Avançados (Institute for Advanced Studies), the Instituto Militar de Engenharia – IME (Military Institute of Engineering), the Instituto Tecnológico de Aeronáutica – ITA (Aeronautics Institute of Technology), Instituto de Pesquisas e Desenvolvimento – IP&D da Universidade do Vale do Paraíba – Univap (Heterogeneous Catalysis Laboratory, Research and Development Institute, University of Vale do Paraíba). This work was also funded by CNPq (grant no. 405624/2022-0) and FINEP (grant no. 25670-SUB-1).

CONFLICT OF INTEREST

The authors declare that there were no conflicts of interest in this paper, including ongoing research and other potential conflicts of interest.

REFERENCES

Amanov, A., & Pyun, Y.-S. (2017). Local heat treatment with and without ultrasonic nanocrystal surface modification of Ti-6Al-4V alloy: Mechanical and tribological properties. *Surface and Coatings Technology*, *326*, 343–354. https://doi.org/10.1016/j.surfcoat.2017.07.064

American Society for Testing & Materials. (2014). *ASTM F136*: *Wrought Titanium-6Aluminum-4Vanadium ELI (Extra Low Interstitial) Alloy for Surgical Implant Applications (UNSR56401).* https://doi.org/10.1520/F0136-13R21E01

Bartkowski, D., Matysiak, W., & Wojtko, K. (2018). Stellite-6 surface layers reinforced with hard and refractory WC particles produced on steel for metal forming. *IOP Conference Series: Materials Science and Engineering*, *393*, 012093. https://doi.org/10.1088/1757-899X/393/1/012093

Callister Jr. W. D., & Rethwisch, D. G. (2014). *Materials science and engineering an introduction* (9. ed.). John Wiley & Sons.

Chagas, D. C. (2016). *Deposition of NiCrAlY on Inconel 718 by CO2 laser*. [Thesis Master on Science], Space Sciences and Technologies, Applied Physics and Mathematics of Technological Institute of Aeronautics.

Dhanda, M., Haldar, B., & Saha, P. (2014). Development and Characterization of Hard and Wear Resistant MMC Coating on Ti-6Al-4V Substrate by Laser Cladding. *Procedia Materials Science*, *6*, 1226–1232. https://doi.org/10.1016/j.mspro.2014.07.196

Duley, W. W. (1976). *CO_2 lasers: Effects and applications*. Academic Press.

Dutta Majumdar, J., & Manna, I. (2011). Laser material processing. *International Materials Reviews*, *56*(5–6), 341–388. https://doi.org/10.1179/1743280411Y.0000000003

El-Hamid, H. K. A., Gaber, A. A., Ngida, R. E. A., Sadek, H. E. H., Khattab, R. M., & Mandour, H. S. (2024). Study of microstructure and corrosion behavior of nano-Al2O3 coating layers on TiO2 substrate via polymeric method and microwave combustion. *Scientific Reports*, *14*(1), 18417. https://doi.org/10.1038/s41598-024-68566-6

European Committee for Standardization. (2018). *BS EN 9100*: 2018. *Quality management systems - Requirements for aviation, space and defense organizations*. CEN.

Figueira, G., R.A.M. Montuori, G.Y. Koga, & P. Gargarella. (2022). Aplicando a otimização de parâmetros para Fusão em Leito de Pó a Laser (L-PBF) ao processamento do aço inoxidável austenítico 316L. *Anais do NOXCORR 2022 - Seminário Brasileiro de Aços Inoxidáveis como Solução Contra Corrosão*, Instituto de Pesquisas Tecnológicas, São Paulo. IPT.

Goodarzi, D. M., Pekkarinen, J., & Salminen, A. (2015). Effect of process parameters in laser cladding on substrate melted areas and the substrate melted shape. *Journal of Laser Applications*, *27*(S2), S29201. https://doi.org/10.2351/1.4906376

Guo, C., Chen, J., Zhou, J., Zhao, J., Wang, L., Yu, Y., & Zhou, H. (2012). Effects of WC–Ni content on microstructure and wear resistance of laser cladding Ni-based

alloys coating. *Surface and Coatings Technology*, *206*(8–9), 2064–2071. https://doi.org/10.1016/j.surfcoat.2011.06.005

Jardim, V. R. (2020). *Characterization of laser deposited tungsten carbide coating on titanium alloy TI-6AL-4V*. [Thesis Doctor on Science, Space Sciences and Technologies, Applied Physics and Mathematics of Technological Institute of Aeronautics].

Jeyaprakash, N., Yang, C.-H., & Sivasankaran, S. (2019). Laser cladding process of Cobalt and Nickel based hard-micron-layers on 316L-stainless-steel-substrate. *Materials and Manufacturing Processes*, *35*(2), 142–151. https://doi.org/10.1080/10426914.2019.1692354

Kaufmann, M., Zenkert, D., & Mattei, C. (2008). Cost optimization of composite aircraft structures including variable laminate qualities. *Composites Science and Technology*, *68*(13), 2748–2754. https://doi.org/10.1016/j.compscitech.2008.05.024

Kim, C.-S., & Rohrer, G. S. (2004). Geometric and Crystallographic Characterization of WC Surfaces and Grain Boundaries in WC-Co Composites. *Interface Science*, *12*(1), 19–27. https://doi.org/10.1023/B:INTS.0000012291.81411.dc

Krawitz, A. D. (1985). The use of X-ray stress analysis for WC-base cermets. *Materials Science and Engineering*, *75*(1–2), 29–36. https://doi.org/10.1016/0025-5416(85)90175-2

Kümmel, D., Linsler, D., Schneider, R., & Schneider, J. (2020). Surface engineering of a titanium alloy for tribological applications by nanosecond-pulsed laser. *Tribology International*, *150*, 106376. https://doi.org/10.1016/j.triboint.2020.106376

Lassner, E., & Schubert, W. (1999). *Titanium and Titanium Alloys: Fundamentals and Applications* (1. ed.). Wiley.

Li, L., Wang, D., Song, W., Gong, J., Hu, Q., & Zeng, X. (2020). Microstructures and mechanical properties of WCP/Ti-6Al-4V composite coatings by laser melt injection and laser-induction hybrid melt injection. *Surface and Coatings Technology*, *385*, 125371. https://doi.org/10.1016/j.surfcoat.2020.125371

Lin, Y.-C., & Lin, Y.-C. (2011). Microstructure and tribological performance of Ti–6Al–4V cladding with SiC powder. *Surface and Coatings Technology*, *205*(23–24), 5400–5405. https://doi.org/10.1016/j.surfcoat.2011.06.001

Lisiecki, A., & Klimpel, A. (2008). Diode laser surface modification of Ti6Al4V alloy to improve erosion wear resistance. *Archives of Materials Science and Engineering*, *32*(1). http://www.amse.acmsse.h2.pl/vol32_1/3211.pdf

Makurat-Kasprolewicz, B., & Ossowska, A. (2023). Electrophoretically deposited titanium and its alloys in biomedical engineering: Recent progress and remaining

challenges. *Journal of Biomedical Materials Research Part B: Applied Biomaterials*, *112*(1), e35342. https://doi.org/10.1002/jbm.b.35342

Marques, C. M. F. G., Bobrovnitchii, G. S., & Holanda, J. N. F. (2013). Análise de fases por difração de raios X de WC-10%Co dopado com terras-raras obtido sob alta pressão. *Matéria (Rio de Janeiro)*, *18*(1), 10–18. https://doi.org/10.1590/S1517-70762013000100003.

Moskalewicz, T., Wendler, B., Zimowski, S., Dubiel, B., & Czyrska-Filemonowicz, A. (2010). Microstructure, micro-mechanical and tribological properties of the nc-WC/a-C nanocomposite coatings magnetron sputtered on non-hardened and oxygen hardened Ti–6Al–4V alloy. *Surface and Coatings Technology*, *205*(7), 2668–2677. https://doi.org/10.1016/j.surfcoat.2010.10.039

Obadele, B. A., Andrews, A., Mathew, M. T., Olubambi, P. A., & Pityana, S. (2015). Improving the tribocorrosion resistance of Ti6Al4V surface by laser surface cladding with TiNiZrO 2 composite coating. *Applied Surface Science*, *345*, 99–108. https://doi.org/10.1016/j.apsusc.2015.03.152

Pawlowski, L. (2008). *The Science and Engineering of Thermal Spray Coatings* (2a. ed.). Willey.

Rominiyi, A. L., & Mashinini, P. M. (2024). A critical review of microstructure and mechanical properties of laser welded similar and dissimilar titanium alloy joints. *Journal of Advanced Joining Processes*, *9*, 100191. https://doi.org/10.1016/j.jajp.2024.100191

Santos, J. C. G. (2014). Structuring and deposition of MCrAlY on stainless steel by laser methods. In *Proceedings of the III Institute of Advanced Studies Symposium on Science and Technology.* SICT-IEAv.

Silva, S. A., Jardim, V. R., Dyer, P. P. O. L., & De Vasconcelos, G. (2024). Structural characterization of tungsten carbide (WC) coatings deposited on 4340 steels by CO2 laser irradiation. *Revista Univap*, *30*(67). https://doi.org/10.18066/revistaunivap.v30i67.4451

Steen, W. M., & Mazumder, J. (2010). *Laser Material Processing* (4. ed.). Springer.

Teixeira, A. C. G. (2016). *Characterisation of Thermo-Electrical Properties of Carbide*. [Thesis Master on Materials Engineering, on Lisbon Technical Institute of Lisbon University].

Teleginski, V. (2016). *CO_2 laser deposition of coatings for thermal protection of aeronautical and industrial turbine blades*. [Thesis Doctor on Science, Space Sciences and Technologies, Applied Physics and Mathematics of Technological Institute of Aeronautics].

Tijo, D., & Masanta, M. (2017). Mechanical performance of in-situ TiC-TiB2 composite coating deposited on Ti-6Al-4V alloy by powder suspension electro-

discharge coating process. *Surface & Coatings Technology*, 328 p. 192–203. http://dx.doi.org/10.1016/j.surfcoat.2017.08.048

Ulusoy, U. (2023). A Review of Particle Shape Effects on Material Properties for Various Engineering Applications: From Macro to Nanoscale. *Minerals*, *13*(1), 91. https://doi.org/10.3390/min13010091

Upadhyaya, G. S. (1999). *Cemented Tungsten Carbides: Production, Properties and Testing* (1. ed.). William Andrew.

Vinayo, M. E., Kassabji, F., Guyonnet, J., & Fauchais, P. (1985). Plasma sprayed WC–Co coatings: Influence of spray conditions (atmospheric and low pressure plasma spraying) on the crystal structure, porosity, and hardness. *Journal of Vacuum Science & Technology A: Vacuum, Surfaces, and Films*, *3*(6), 2483–2489. https://doi.org/10.1116/1.572863

Volu, R. M., Zilnyk, K., Dyer, S. A. S., Santos, C. L. D., Jakutis Neto, J., & Vasconcelos, G. D. (2023). A New Two-Step Method for Laser Cladding of Silicon Carbide in Wc-Co Substrates. *Materials Research*, *26*, e20220195. https://doi.org/10.1590/1980-5373-mr-2022-0195

Wang, D. S., Tian, Z. J., Shen, L. D., & Huang, Y. H. (2013). Preparation of Thick Ceramic Coating by Laser Multi-Layer Cladding I - Crack Control. *Advanced Materials Research*, *785–786*, 906–909. https://doi.org/10.4028/www.scientific.net/AMR.785-786.906

Weng, F., Chen, C., & Yu, H. (2014). Research status of laser cladding on titanium and its alloys: A review. *Materials & Design*, *58*, 412–425. https://doi.org/10.1016/j.matdes.2014.01.077

Yetim, A. F., Celik, A., & Alsaran, A. (2010). Improving tribological properties of Ti6Al4V alloy with duplex surface treatment. *Surface and Coatings Technology*, *205*(2), 320–324. https://doi.org/10.1016/j.surfcoat.2010.06.048

Zhao, H., Zhao, C., Xie, W., Wu, D., Du, B., Zhang, X., Wen, M., Ma, R., Li, R., Jiao, J., Chang, C., Yan, X., & Sheng, L. (2023). Research Progress of Laser Cladding on the Surface of Titanium and Its Alloys. *Materials*, *16*(8), 3250. https://doi.org/10.3390/ma16083250

Zhao, Y., Sun, J., & Li, J. (2015). Study on crack sensitivity and tribological characterisation of functionally gradient material multi-layer by laser cladding with powder mixture of Ni-based alloy and tungsten carbide. *International Journal of Surface Science and Engineering*, *9*(4), 370. https://doi.org/10.1504/IJSURFSE.2015.070814

Zwerdeling R. (2013). Operational austerity. *AERO Magazine*, (228). https://aeromagazine.uol.com.br/artigo/austeridade-operacional_970.html